

Chapter 2

Circular integrated optical microresonators: Analytical methods and computational aspects

Kirankumar Hiremath

Department of Mathematics, Institute for Scientific Computing and Mathematical Modeling, University of Karlsruhe, Karlsruhe, Germany

hiremath@math.uni-karlsruhe.de

and

Manfred Hammer

Department of Applied Mathematics, MESA⁺ Institute for Nanotechnology, University of Twente, Enschede, The Netherlands

m.hammer@math.utwente.nl

Abstract This chapter discusses an ab-initio frequency-domain model of circular microresonators, built on the physical notions that commonly enter the description of the resonator functioning in terms of interaction between fields in the circular cavity with the modes supported by the straight bus waveguides. Quantitative evaluation of this abstract model requires propagation constants associated with the cavity/bend segments, and scattering matrices, that represent the wave interaction in the coupler regions. These quantities are obtained by an analytical (2-D) or numerical (3-D) treatment of bent waveguides, along with spatial coupled mode theory (CMT) for the couplers. The required CMT formulation is described in detail. Also, quasi-analytical approximations for fast and accurate computation of the resonator spectra are discussed. The formalism discussed in this chapter provides valuable insight in the functioning of the resonators, and it is suitable for practical device design.

2.1 Introduction

Resonances in optical microcavities are explored for a variety of applications [1, 2, 3]. Single or cascaded microresonators not only in the form of rings, disks, spheres, but also in other forms like squares, rectangles, or flowerlike microgears (disks with angularly periodically varying radii), and arranged in various configurations, led to a multitude of interesting phenomena [4, 5]. In this chapter we focus on the most common microresonator configuration applied in integrated optics, consisting of a ring- or disk-shaped cavity which is evanescently coupled to two parallel bus waveguides.

Quite frequently the functioning of these resonators is discussed on the basis of a frequency domain model [6, 7, 8], where the interaction between the cavity and the straight waveguides is represented in terms of scattering matrices for the coupler regions. Interferometric resonances are established by segments of bent waveguides

that connect these couplers. By treating the coupler scattering matrices and the bend mode propagation constants associated with the cavity as free parameters, one can estimate the response of the microresonators [9, 10, 11].

As a step beyond, one might try to solve the parametric model from first principles, i.e. calculate all parameter values for given geometry and material properties. Although this is obviously essential for realistic device design, rather few ab-initio studies of that kind exist so far. Initial attempts can be found in Refs. [12, 13, 14], which differ with respect to the methods and approximations that are employed to obtain the modal basis solutions for the curved cavity segments, and to predict the interaction between the cavity and the bus waveguides. For the latter task, approaches based on coupled mode theory (CMT) [15, Secs. 1.4, 4.2.4], [16] are applied.

The CMT arguments in the former studies are basically derived for the interaction of parallel straight waveguides, and can be extended to low loss cavities (typically very large radius and/or high index contrast). But the situation is characteristically different for cavity modes with non-negligible losses. It is possible to reformulate the CMT approach to overcome the above shortcomings [17, 18]. The simulations rely on frequency domain modal solutions for bent waveguides and curved interfaces on radially unbounded domains, which can be computed analytically for the 2-D setting [19]. In 3-D, numerical means have to be employed, like e.g. the film mode matching method [20]. For given real frequency, these modal solutions have complex angular propagation constants with a suitably fast decay in the radial direction [19], such that they can be conveniently used as basis fields in the frequency domain coupled mode description. The coupled mode equations can be derived from a variational principle [17] or by means of reciprocity techniques [21]. This leads to an ab-initio frequency domain spatial CMT model of circular microresonators which is a straightforward implementation of the conventional traveling wave microresonator viewpoint [8, 9].

Once facilities for determining bend mode propagation constants and coupler scattering matrices are at hand, adaptation of the model to different configurations should be relatively simple, requiring merely modifications in the initial analytical reasoning. This concerns e.g. cavity shapes with piecewise straight segments (“racetrack” resonators [22]), resonators with only a single bus waveguide for resonant phase shifting [23] or with perpendicular bus waveguide cores [24]. For cases like the coupled optical resonator waveguides [25] where the intercavity coupling needs to be taken into account, a CMT formalism as in Sec. 2.4 with bend modes of the two cavities as basis fields would be required. Extension to larger composites with parallel coupled cavities [26, 27], serial configurations [26, 28], or even mesh-like filters [24, 29, 30] should be straightforward by means of scattering matrix operations, given the input-output characteristics of the single-cavity resonator elements.

The present approach differs from models based on time domain modes for the entire circular cavities [26, 31]. These are solutions with integer angular mode number and complex eigen-frequency [12, 32]. Due to their radially growing fields, they are not directly suitable for the frequency domain CMT framework. Therefore we

use the frequency domain model of the bent waveguides as discussed in Sec. 2.3. As these modal solutions have complex valued angular mode numbers, they do not constitute valid solutions for the full rotationally symmetric cavities, and hence are not useful to access directly the (complex) resonance frequencies of the isolated cavities. Still, by taking into account their interaction with the straight waveguides, one can construct approximate solutions for the system “cavity + bus waveguides” at given wavelengths, and thereafter estimate resonance frequencies. It is possible to translate between both viewpoints [12, 32].

Alternatively, rigorous numerical tools can be employed to model the resonators. The most prominent among these are the finite difference time domain (FDTD) method [33, 34, 35], and its (discontinuous Galerkin) finite-element variants [36, 37, 38]. However, already in the 2-D setting these simulations turn out to be inconveniently time consuming; the computational effort required in 3-D is expected, at least at present, to be prohibitive for practical design work. Integral equation methods are also applied for efficient analytical solutions of eigenvalue and scattering problems for specific 2-D configurations of micro-ring and disk cavities [39, 40, 41]. Unfortunately, the extension to 3-D appears to be far from obvious.

In the subsequent sections, we discuss the coupled mode theory approach in detail. Sec. 2.2 describes the “standard” resonator model formulated directly for multimodal cavities. Evaluation of the abstract equations requires propagation constants of the relevant cavity modes, and the coupler scattering matrices. These quantities are relatively easy to obtain in a 2-D setting, where also rigorous numerical data suitable for reliable benchmarking is conveniently available. The 2-D configurations might also be of interest as effective-index projections of actual 3-D structures [13]. Therefore we first discuss in detail 2-D configurations of bent waveguides in Sec. 2.3 and couplers in Sec. 2.4. Numerical approaches for the efficient evaluation of the resonator spectrum are presented in Sec. 2.5. In Sec. 2.6 these ingredients are combined to simulate full 2-D microresonators; the extension to three spatial dimensions follows in Sec. 2.7. In both cases the CMT results are compared with data from other independent numerical methods. Conclusions of the present analysis are given in Sec. 2.8.

2.2 Analytical framework

Consider a microresonator consisting of a ring- or disk shaped dielectric cavity, evanescently coupled to two parallel straight waveguides. In the laterally coupled configuration (Fig. 2.1, left; a top view of a real 3-D device, also the 2-D setting of Secs. 2.3–2.6), these waveguides are placed in the x - z -plane just as the cavity is, whereas in the vertically coupled configuration (Fig. 2.1, right), they are positioned at different y levels. Each of these configurations has its own advantages and disadvantages [10].

We chose a frequency domain description, where a time-harmonic optical signal $\sim \exp(i\omega t)$ of given real frequency ω corresponding to vacuum wavelength λ is

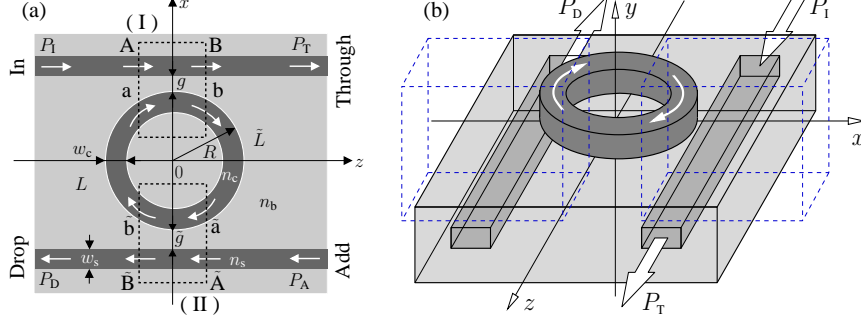


Fig. 2.1 The “standard” microresonator model : A laterally (a) or a vertically (b) coupled resonator is functionally decomposed into two bent-straight waveguide couplers (I) and (II), which are interconnected by cavity segments of lengths L and \tilde{L} outside the couplers. Schematics for the laterally coupled resonator (a): A cavity of radius R , core refractive index n_c and width w_c is placed between two straight waveguides with core refractive index n_s and width w_s , with gaps of width g and \tilde{g} between the cavity and the waveguides. The cladding refractive index is n_b (Illustrations taken from Ref.[17, 18]).

present everywhere. In line with the most common view on circular microcavities [8, 9], the resonators are functionally divided into two bent-straight waveguide couplers, which are connected to each other by segments of the cavity. Semi-infinite pieces of straight waveguides constitute the external connections, where the letters $A, B, \tilde{A}, \tilde{B}$ (external) and $a, b, \tilde{a}, \tilde{b}$ (internal) denote the coupler ports.

Assume that the interaction between the optical waves in the cavity and in the bus waveguides is negligible outside the coupler regions. Also assume that all transitions inside the couplers are sufficiently adiabatic, such that back reflections do not play a significant role for the resonator functioning. We further restrict the model to unidirectional wave propagation, as indicated by the arrows in Fig. 2.1. Depending on the specific configuration, these assumptions can be justified or not; for the examples in Secs. 2.6, 2.7 they appear to be adequate.

Suppose that the straight waveguides supports N_s guided modes with propagation constants β_{sq} , $q = 1, \dots, N_s$. For the cavity, N_b bend modes are taken into account. Due to the curvature, their propagation constants $\gamma_{bp} = \beta_{bp} - i\alpha_{bp}$, $p = 1, \dots, N_b$, are complex valued [19]. Here β_{bp} and α_{bp} are positive real valued quantities representing phase constants and attenuation constants of the cavity modes. All these modes are power normalized. Let the variables A_q, B_q , and a_p, b_p , denote the directional amplitudes of the properly normalized ‘forward’ propagating (clockwise direction, cf. Fig. 2.1) basis modes in the respective coupler port planes, combined into amplitude (column) vectors \mathbf{A}, \mathbf{B} , and \mathbf{a}, \mathbf{b} .

Then the response of coupler (I) can be represented in terms of its scattering matrix, which relates the amplitudes of the outgoing waves to the amplitudes of the corresponding incoming modes as

$$\begin{pmatrix} \mathbf{a}^- \\ \mathbf{A}^- \\ \mathbf{b} \\ \mathbf{B} \end{pmatrix} = \begin{pmatrix} 0 & 0 & \mathbf{S}_{bb}^- & \mathbf{S}_{bs}^- \\ 0 & 0 & \mathbf{S}_{sb}^- & \mathbf{S}_{ss}^- \\ \mathbf{S}_{bb} & \mathbf{S}_{bs} & 0 & 0 \\ \mathbf{S}_{sb} & \mathbf{S}_{ss} & 0 & 0 \end{pmatrix} \begin{pmatrix} \mathbf{a} \\ \mathbf{A} \\ \mathbf{b}^- \\ \mathbf{B}^- \end{pmatrix}. \quad (2.1)$$

Here the superscripts $-$ indicate the amplitudes of backward (anticlockwise) propagating waves, and the zeroes implement the assumption of negligible back-reflections. The entries of the submatrices \mathbf{S}_{vw} with $v, w = b, s$ represent the ‘coupling’ from a particular mode of the waveguide w to a particular mode of the waveguide v .

A fundamental property of any linear circuit made of nonmagnetic materials is that the transmission between any two ‘ports’ does not depend upon the propagation direction, i.e. the full scattering matrix of the reciprocal circuit is symmetric [15, Sec. 1.3.2]. This argument even holds for circuits with attenuating materials, in the presence of radiative losses, and irrespective of the particular shape of the connecting cores. It relies crucially on the precise definition of the ‘ports’ of the circuit, where independent ports can be realized either by mode orthogonality or by spatially well separated outlets.

Assuming that the above reciprocity requirements are satisfied for the bent-straight waveguide couplers, one expects that the bidirectional coupler scattering matrix is symmetric (as we shall see in Secs. 2.4.4, 2.4.5, Figs. 2.6–2.9, the numerical results give evidence that this is indeed the case). For the submatrices this implies that the following equalities hold (T denotes the transpose):

$$\mathbf{S}_{bb} = (\mathbf{S}_{bb}^-)^T, \quad \mathbf{S}_{sb} = (\mathbf{S}_{bs}^-)^T, \quad \mathbf{S}_{bs} = (\mathbf{S}_{sb}^-)^T, \quad \mathbf{S}_{ss} = (\mathbf{S}_{ss}^-)^T. \quad (2.2)$$

If coupler (I) is defined symmetrical with respect to the central plane $z = 0$, and if identical mode profiles are used for the incoming and outgoing fields, then one can further expect the transmissions from \mathbf{A} to \mathbf{b} to be equal to the transmission from \mathbf{B}^- to \mathbf{a}^- [15, Sec. 1.3.2]. Similarly, the transmissions from \mathbf{a} to \mathbf{B} and from \mathbf{b}^- to \mathbf{A}^- are equal:

$$\mathbf{S}_{bs} = \mathbf{S}_{bs}^-, \quad \mathbf{S}_{sb} = \mathbf{S}_{sb}^-. \quad (2.3)$$

As a result of (2.2) and (2.3), also the unidirectional scattering matrix

$$\mathbf{S} = \begin{pmatrix} \mathbf{S}_{bb} & \mathbf{S}_{bs} \\ \mathbf{S}_{sb} & \mathbf{S}_{ss} \end{pmatrix} \quad (2.4)$$

associated with the clockwise propagation through coupler (I) is symmetric:

$$\mathbf{S}_{bs} = (\mathbf{S}_{sb})^T, \quad \mathbf{S}_{ss}^- = (\mathbf{S}_{bb}^-)^T. \quad (2.5)$$

The physical interpretation of the above statements is that ‘the coupling from the straight waveguide to the cavity is equal to the coupling from the cavity bend to the bus waveguide’.

A completely analogous reasoning applies to the second coupler, where the tilde \sim identifies the mode amplitudes $\tilde{\mathbf{A}}, \tilde{\mathbf{B}}$, and $\tilde{\mathbf{a}}, \tilde{\mathbf{b}}$ at the port planes, and the unidirectional scattering matrix $\tilde{\mathbf{S}}$ related to coupler (II), such that the coupler operation is

represented as

$$\begin{pmatrix} \mathbf{b} \\ \mathbf{B} \end{pmatrix} = \mathbf{S} \begin{pmatrix} \mathbf{a} \\ \mathbf{A} \end{pmatrix}, \quad \begin{pmatrix} \tilde{\mathbf{b}} \\ \tilde{\mathbf{B}} \end{pmatrix} = \tilde{\mathbf{S}} \begin{pmatrix} \tilde{\mathbf{a}} \\ \tilde{\mathbf{A}} \end{pmatrix}. \quad (2.6)$$

Outside the coupler regions the bend modes are used for the description of the field propagating in the cavity, with the angular / arc-length dependence given by their propagation constants (cf. (2.20)). Hence the amplitudes at the entry and exit ports of the connecting cavity segments are related to each other as

$$\mathbf{a} = \mathbf{G}\tilde{\mathbf{b}} \quad \text{and} \quad \tilde{\mathbf{a}} = \tilde{\mathbf{G}}\mathbf{b}, \quad (2.7)$$

where \mathbf{G} and $\tilde{\mathbf{G}}$ are $N_b \times N_b$ diagonal matrices with entries $G_{p,p} = \exp(-i\gamma_{bp}L)$ and $\tilde{G}_{p,p} = \exp(-i\gamma_{bp}\tilde{L})$, respectively, for $p = 1, \dots, N_b$.

We are interested in the case where modal powers $P_{Iq} = |A_q|^2$ and $P_{Aq} = |\tilde{A}_q|^2$ are given at the input port A and at the add port \tilde{A} of the resonator, and we need to calculate the transmitted power $P_{Tq} = |B_q|^2$ at port B and the backward dropped power $P_{Dq} = |\tilde{B}_q|^2$ at port \tilde{B} . This is equivalent to solving the linear system established by (2.6) and (2.7) for \mathbf{B} and $\tilde{\mathbf{B}}$ in terms of \mathbf{A} and $\tilde{\mathbf{A}}$. Due to the linearity of the device the restriction to an excitation in only one port, here port A, with no incoming add-signal $\tilde{\mathbf{A}} = \mathbf{0}$, is sufficient. Then one obtains

$$\mathbf{B} = (\mathbf{S}_{sb}\mathbf{G}\tilde{\mathbf{S}}_{bb}\tilde{\mathbf{G}}\Omega^{-1}\mathbf{S}_{bs} + \mathbf{S}_{ss})\mathbf{A}, \quad \tilde{\mathbf{B}} = (\tilde{\mathbf{S}}_{sb}\tilde{\mathbf{G}}\Omega^{-1}\mathbf{S}_{bs})\mathbf{A} \quad (2.8)$$

for amplitudes of the outgoing guided modes in the through- and drop-ports, and

$$\mathbf{b} = \Omega^{-1}\mathbf{S}_{bs}\mathbf{A}, \quad \tilde{\mathbf{b}} = \tilde{\mathbf{S}}_{bb}\tilde{\mathbf{G}}\Omega^{-1}\mathbf{S}_{bs}\mathbf{A} \quad (2.9)$$

for the internal mode amplitudes in the cavity, where $\Omega = \mathbf{I} - \mathbf{S}_{bb}\mathbf{G}\tilde{\mathbf{S}}_{bb}\tilde{\mathbf{G}}$.

The spectral response of the resonator is found by computing the transmitted (P_{Tq}) and dropped (P_{Dq}) power for a series of wavelengths with the help of (2.8). Resonances manifest as peaks in P_{Dq} along with simultaneous dips in P_{Tq} . The pronounced wavelength dependence at the resonance is caused by the “resonance denominator” Ω . For further insight, consider (2.8) and (2.9) when Ω is singular, i.e. it has an eigenvalue zero, or, equivalently, when $\mathbf{S}_{bb}\mathbf{G}\tilde{\mathbf{S}}_{bb}\tilde{\mathbf{G}}$ has a unit eigenvalue. This corresponds to a cavity field which reproduces itself after propagating consecutively along the right cavity segment, through coupler (II), along the left cavity segment, and finally through coupler (I). The self-consistent reproduction of the cavity field represents the *resonance condition* in the present abstract multimode cavity model.

Practical evaluation of the — so far only parameterized — equations (2.8) and (2.9) requires values for the phase and attenuation constants $\gamma_{bp} = \beta_{bp} - i\alpha_{bp}$ of the cavity modes, contained in \mathbf{G} , $\tilde{\mathbf{G}}$, and the scattering matrices \mathbf{S} , $\tilde{\mathbf{S}}$ of couplers (I) and (II). Corresponding procedures will be the subject of the following sections, where the concepts are first discussed in 2-D, then extended to the full 3-D setting.

2.2.1 Monomodal resonators

For fully symmetric microresonators (i.e. identical couplers (I), (II), connected by equal cavity segments $\tilde{\cdot} = \cdot$) with single mode cavity and bus cores, further evaluation of expressions (2.8) and (2.9) is fairly standard [8, 9]. Let $S_{bb} = |S_{bb}| e^{i\varphi}$, $S_{ss} - S_{bs}S_{sb}/S_{bb} = \rho e^{i\psi}$ with φ, ρ and ψ real. Then the dropped power is given by

$$P_D = P_1 \frac{|S_{sb}|^2 |S_{bs}|^2 e^{-\alpha L_{\text{ext}}}}{1 + |S_{bb}|^4 e^{-2\alpha L_{\text{ext}}} - 2|S_{bb}|^2 e^{-\alpha L_{\text{ext}}} \cos(\beta L_{\text{ext}} - 2\varphi)}, \quad (2.10)$$

and the expression for the through power reads

$$P_T = P_1 \frac{|S_{ss}|^2 (1 + |S_{bb}|^2 \rho^2 e^{-2\alpha L_{\text{ext}}} - 2|S_{bb}| \rho e^{-\alpha L_{\text{ext}}} \cos(\beta L_{\text{ext}} - \varphi - \psi))}{1 + |S_{bb}|^4 e^{-2\alpha L_{\text{ext}}} - 2|S_{bb}|^2 e^{-\alpha L_{\text{ext}}} \cos(\beta L_{\text{ext}} - 2\varphi)}. \quad (2.11)$$

Here $L_{\text{ext}} = L + \tilde{L}$ is the total length of those parts of the cavity which are not already included in the couplers. β and α are the phase and attenuation constants of the single relevant bend mode of the cavity.

In principle, all quantities in (2.10) and (2.11) are wavelength dependent. Hence the rigorous way to determine the resonator spectrum would be to evaluate all relevant quantities for a series of wavelengths. Some further insight, however, can be obtained with the approximation that significant changes in the drop and through power, on a limited wavelength interval, originate exclusively from the cosine terms in (2.10) and (2.11) that include the phase information (this term corresponds to the resonance denominator Ω in (2.8) and (2.9)).

To take into account some non-negligible length l of the cavity segments in the coupler regions, write the phase term as $\beta L_{\text{ext}} - 2\varphi = \beta L_{\text{cav}} - \phi$, where $L_{\text{cav}} = 2\pi R$ is the complete cavity length, and $\phi = 2\beta l + 2\varphi$ (a corresponding procedure is also applied to the phase term in the numerator of (2.11)). Further consider only the wavelength dependence of the phase constant β as it appears explicitly in the term $\beta L_{\text{cav}} - \phi$. In this way, one incorporates the wavelength dependence of the phase change βL_{cav} for the entire cavity, but disregards the wavelength dependence of the phase change ϕ that is introduced by the interaction with the port waveguides.

Resonances (i.e. maxima of the dropped power) are now characterized by singularities in the denominators of (2.10), (2.11), which occur when $\cos(\beta L_{\text{cav}} - \phi) = 1$, i.e. when the total phase gain after one cavity round trip is a multiple of 2π . This leads to the *resonance condition*

$$\beta = \frac{2m\pi + \phi}{L_{\text{cav}}} =: \beta_m, \quad \text{for integer } m. \quad (2.12)$$

For a resonant configuration, the *dropped power* is given by

$$P_D|_{\beta=\beta_m} = P_1 \frac{|S_{sb}|^2 |S_{bs}|^2 e^{-\alpha L_{\text{ext}}}}{(1 - |S_{bb}|^2 e^{-\alpha L_{\text{ext}}})^2}. \quad (2.13)$$

Note that properly computed values of S_{sb} , S_{bs} and S_{bb} already include the losses along the parts of the cavity inside the couplers. Therefore L_{ext} in (2.13) (and in those places of (2.10), (2.11) where attenuation is concerned) must not be replaced by L_{cav} .

For the present case of monomodal resonators, one can now derive the following familiar expressions that characterize the resonances [8]. Here we only summarize the results.

- The *free spectral range (FSR)* $\Delta\lambda$ is defined as the wavelength difference between two successive maxima of the dropped power (or minima of the through power) and is given by

$$\Delta\lambda \approx \frac{\lambda^2}{n_{\text{eff}}L_{\text{cav}}} \Big|_m \quad (2.14)$$

where λ is the resonance wavelength of the m -th order resonance, and $n_{\text{eff}} = \lambda\beta_m/2\pi$ is the effective mode index of the cavity mode. Here we assumed that the effective group index is equal to the effective index.

- The *full width at half maximum (FWHM)* $2\delta\lambda$ measures the width of the resonance peak at a level of half the resonance value, i.e. the sharpness of the peak. For the resonance of order m one obtains

$$2\delta\lambda = \frac{\lambda^2}{\pi L_{\text{cav}} n_{\text{eff}}} \Big|_m \left(\frac{1}{|S_{bb}|} e^{\alpha L/2} - |S_{bb}| e^{-\alpha L/2} \right). \quad (2.15)$$

- The ratio of the FSR and the FWHM at a specific resonance is called the *finesse* F :

$$F = \frac{\Delta\lambda}{2\delta\lambda} = \pi \frac{|S_{bb}| e^{-\alpha L/2}}{1 - |S_{bb}|^2 e^{-\alpha L}}. \quad (2.16)$$

- The *quality factor* Q can be viewed as the ability of the cavity to confine the field in space or time, which determines the sharpness of the resonance peaks. It is defined here ¹ as the ratio of the resonance wavelength to the FWHM

$$Q = \frac{\lambda}{2\delta\lambda} = \pi \frac{n_{\text{eff}} L_{\text{cav}}}{\lambda} \frac{|S_{bb}| e^{-\alpha L/2}}{1 - |S_{bb}|^2 e^{-\alpha L}} = \frac{n_{\text{eff}} L_{\text{cav}}}{\lambda} F. \quad (2.17)$$

Hence, for a circular resonator with radius R and cavity length $L_{\text{cav}} = 2\pi R$, one obtains $Q = kR n_{\text{eff}} F$ for the relationship between Q and finesse F .

Again, one can improve the accuracy of the above expressions by using the effective group index of the cavity mode in place of the effective mode index n_{eff} [8].

¹ In the time domain, the Q factor $Q = \omega/(2\delta\omega)$ is defined as the ratio of the optical power stored in the cavity to the cycle averaged power radiated out of the cavity [42]. The larger the Q factor, the longer the optical field is trapped inside the cavity.

2.3 Waveguiding along bent cores

An analytical description of bent slab waveguides is apparently well known [15, Sec. 5.2.4], [43, 44], but seemingly hardly ever evaluated rigorously. Bessel- and Hankel-functions of large complex order and large argument are involved. Probably this constitutes a major obstacle, such that most authors resorted to approximations. However, by using uniform asymptotic expansions of the Bessel/Hankel functions, we found that a quite rigorous analytic treatment of the problem is possible [19].

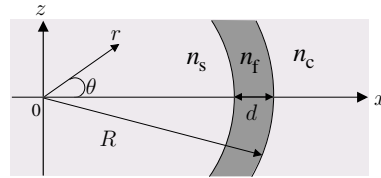
Consider a bent slab waveguide with the y -axis as the axis of symmetry as shown in Fig. 2.2. For the present 2-D treatment, all material properties and the electromagnetic fields are assumed to be invariant in the y direction. Being specified by the radially dependent piecewise constant refractive index $n(r)$, the waveguide can be seen as a structure that is homogeneous along the angular coordinate θ . Hence we choose an ansatz for the bend modes with pure exponential dependence on the azimuthal angle, where the (dimensionless) angular mode number is commonly written as a product γR with a reasonably defined bend radius R , such that γ can be interpreted as a propagation constant. Note that the definition of the bend radius (here the outer rim, as in Fig. 2.2), and consequently the definition of the cavity size, is to some degree arbitrary. The consequences of different choices of R are explained in [19].

In the cylindrical coordinate system (r, θ) , solutions for the optical electric field \mathbf{E} and magnetic field \mathbf{H} are sought in the functional form (in the usual complex notation) of bend modes

$$\begin{pmatrix} \mathbf{E} \\ \mathbf{H} \end{pmatrix}(r, \theta, t) = \begin{pmatrix} (\tilde{E}_r, \tilde{E}_y, \tilde{E}_\theta) \\ (\tilde{H}_r, \tilde{H}_y, \tilde{H}_\theta) \end{pmatrix}(r) e^{i(\omega t - \gamma R \theta)}. \quad (2.18)$$

The tilde indicates the mode profile, γ is the propagation constant of the bend mode. Since the electromagnetic field propagating through the bent waveguide is lossy, $\gamma = \beta - i\alpha$ is complex valued, where β and α are the real valued phase and attenuation constants.

Fig. 2.2 2-D bent slab waveguide. The core of thickness d and refractive index n_f is embedded between an interior medium (‘substrate’) with refractive index n_s and an exterior medium (‘cladding’) with refractive index n_c . The distance between the origin and the *outer rim* of the bend defines the bend radius R (Illustration taken from Ref.[19]).



Inserting the ansatz (2.18) into the Maxwell curl equations, one obtains two decoupled sets of equations: one set for transverse electric (TE) waves with nonzero components \tilde{E}_y , \tilde{H}_r , and \tilde{H}_θ , and a second set for transverse magnetic (TM) waves with nonzero components \tilde{H}_y , \tilde{E}_r , and \tilde{E}_θ . Within radial intervals with constant refractive index n , the principal components $\phi = \tilde{E}_y$ (TE) or $\phi = \tilde{H}_y$ (TM) satisfy a Bessel equation

$$\frac{\partial^2 \phi}{\partial r^2} + \frac{1}{r} \frac{\partial \phi}{\partial r} + (n^2 k^2 - \frac{\gamma^2 R^2}{r^2}) \phi = 0 \quad (2.19)$$

of complex order γR , where $k = 2\pi/\lambda$ is the given real valued vacuum wavenumber.

By solving (2.19) piecewise in radial intervals with constant refractive index, together with polarization dependent material interface conditions and suitable boundary conditions at $r \rightarrow 0$ (bounded solutions) and at $r \rightarrow \infty$ (outgoing fields), one obtains a dispersion equation (transverse resonance condition) for the bent waveguide. For a given frequency ω , discrete values of γ are to be identified as roots of this equation in the complex plane, where we employed numerical means in the form of a secant method. Bessel/Hankel functions with complex order are evaluated on the basis of uniform asymptotic expansions [45].

The outcome is a set of complex bend mode propagation constants with accompanying complex mode profiles. The modes are labeled by the number of radial minima in the absolute value of the principal component. Despite their oscillatory behavior in the outer region, the bend modes can be rigorously power normalized and they satisfy certain orthogonality conditions. We refer to Ref. [19] for further details on the solver and on bend mode properties.

2.3.1 Bend modes

Fig. 2.3 illustrates results of the former procedures. For large bend radius, the bend mode resembles closely the familiar, well confined mode of a symmetric straight slab waveguide. Closer inspection reveals that the tail of the bent mode is protruding more outwards into the cladding region than inwards into the substrate region. For smaller bend radii, the confinement decreases and the relative level of the field in the cladding grows, along with a shift of the absolute field maximum towards the outer rim of the core. With increasing bend radius one observes an almost exponential decrease of the attenuation constant, whereas the phase constant of the bent mode approaches the phase constant of the corresponding straight waveguide mode [19].

The effect of ‘bending’ and the lossy nature of the bend modes are illustrated best by the snapshots of the physical fields in the second row of Fig. 2.3. For the bent waveguide with $R = 3\mu\text{m}$, the radiative tails of the field in the cladding are clearly visible. Just as for straight configurations, the confinement of bend modes depends upon the refractive index contrast; for sufficiently wide waveguides, higher order modes can be supported [19].

2.3.2 Whispering gallery modes

If the core width of a bent waveguide with sufficient curvature is increased, a regime can be reached where the modes are guided by just the outer dielectric interface, while the precise location of the interior interface becomes irrelevant. The model of

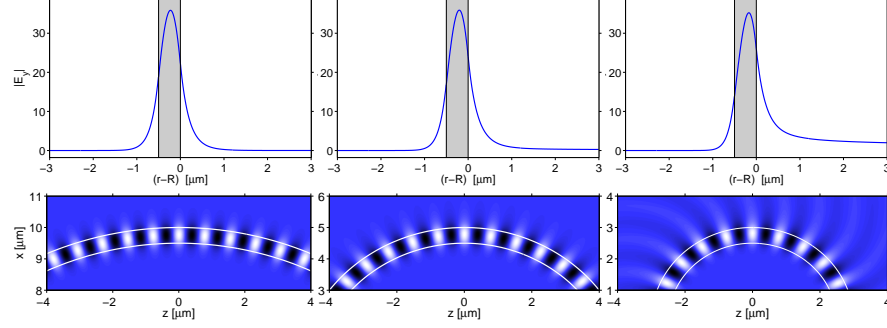


Fig. 2.3 TE_0 mode profiles for bent waveguides with $(n_s, n_f, n_c) = (1.0, 1.5, 1.0)$, $d = 0.5 \mu\text{m}$, $\lambda = 1.05 \mu\text{m}$ for bend radii $R = 10, 5, 3 \mu\text{m}$. First row: radial dependence of the absolute value of the basic electric field component \tilde{E}_y . The profiles are power normalized, with the global phase adjusted such that $\tilde{E}_y(R)$ is real and positive. Second row: snapshots of the propagating bend modes according to (2.18). The gray scales correspond to the levels of the real, physical field E_y . $n_{\text{neff}} = \gamma/k$ are $1.3232 - i 6.4517 \cdot 10^{-11}$, $1.2930 - i 7.5205 \cdot 10^{-6}$, $1.2576 - i 6.8765 \cdot 10^{-4}$ resp.

Sec. 2.3 also covers such configurations with the formal choice $n_s = n_f$ in Fig. 2.2. The solutions are called whispering gallery modes (WGMs). Fig. 2.4 illustrates the first four lowest order WGMs that are supported by a structure with the parameters of the previous bent waveguide segments, where the interior has been filled with the core material. While the fundamental field TE_0 is well confined to the waveguide, the higher order modes spread far beyond the core. Although these modes attenuate fast, we shall see in Sec. 2.6.2 that they can influence the response of a resonator with a cavity made up of the present bend segments.

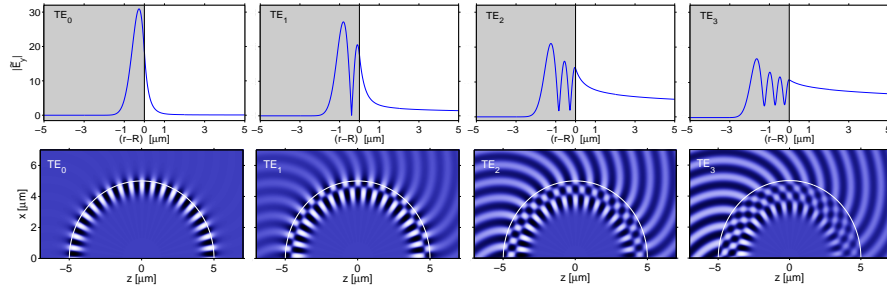


Fig. 2.4 TE polarized whispering gallery modes; the plots show the absolute value $|\tilde{E}_y|$ of the radial mode profile (top) and snapshots of the propagating physical field E_y (bottom). The effective mode indices γ_j/k for bend radius $R = 5 \mu\text{m}$ are $1.32793 - i 9.531 \cdot 10^{-7}$ (TE_0), $1.16931 - i 4.032 \cdot 10^{-4}$ (TE_1), $1.04222 - i 5.741 \cdot 10^{-3}$ (TE_2), and $0.92474 - i 1.313 \cdot 10^{-2}$ (TE_3), for $\lambda = 1.05 \mu\text{m}$. All modes are power normalized.

2.4 Bent-straight waveguide couplers

Capitalizing on the availability of analytical bend modes, we now proceed to the coupler regions. One of the many variants of coupled mode theory (CMT) [15, Secs. 1.4, 4.2.4], [16] will be applied here to model the interaction of the optical waves. The formulation takes into account that multiple modes in each of the cores may turn out to be relevant for the functioning of the resonators [17].

Consider the coupler configuration shown in Fig. 2.5(a). The basis fields for the CMT description are the time-harmonic modal solutions associated with the isolated bent (b) and straight cores (c). In line with the assumptions of Sec. 2.2 only forward propagating modes are considered, where for convenience we choose the z -axis of the Cartesian system as introduced in Fig. 2.5 as the common propagation coordinate for all fields.

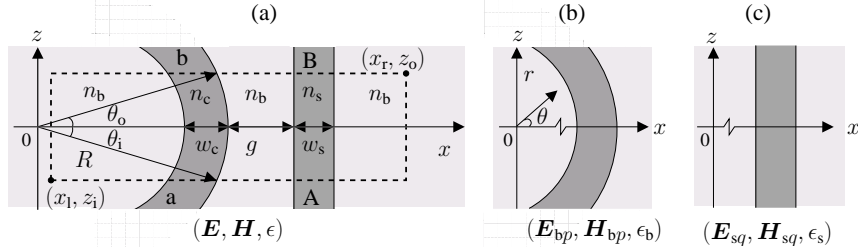


Fig. 2.5 The bent-straight waveguide coupler configuration (a), coupler (I) of Fig. 2.1. The interaction between the modal fields supported by the bent and straight cores is restricted to the computational window $[x_l, x_r] \times [z_l, z_o]$. Inside this region the optical field is represented as a linear combination of the modal fields of the bent waveguide (b) and of the straight waveguide (c) (Illustrations taken from Ref. [17]).

Let \mathbf{E}_{bp} , \mathbf{H}_{bp} , and ϵ_b represent the modal electric fields, magnetic fields, and the spatial distribution of the relative permittivity of the bent waveguide. For the CMT formalism, the bend mode field ansatz (2.18) in the polar coordinates is expressed in the Cartesian x - z -system, such that the basis fields for the cavity read

$$\begin{pmatrix} \mathbf{E}_{bp} \\ \mathbf{H}_{bp} \end{pmatrix}(x, z) = \begin{pmatrix} \tilde{\mathbf{E}}_{bp} \\ \tilde{\mathbf{H}}_{bp} \end{pmatrix}(r(x, z)) e^{-i\gamma_{bp} R \theta(x, z)}. \quad (2.20)$$

Here $\tilde{\mathbf{E}}_{bp}$ and $\tilde{\mathbf{H}}_{bp}$ are the radial dependent electric and magnetic parts of the mode profiles; γ_{bp} are complex valued propagation constants. Consistent with the definition in Sec. 2.3, the bend radius R indicates the position of the outer curved interface (Fig. 2.5).

Similarly, \mathbf{E}_{sq} , \mathbf{H}_{sq} , and ϵ_s denote the modal fields and the relative permittivity associated with the straight waveguide, which are given by

$$\begin{pmatrix} \mathbf{E}_{sq} \\ \mathbf{H}_{sq} \end{pmatrix}(x, z) = \begin{pmatrix} \tilde{\mathbf{E}}_{sq} \\ \tilde{\mathbf{H}}_{sq} \end{pmatrix}(x) e^{-i\beta_{sq} z}. \quad (2.21)$$

Here positive propagation constants β_{sq} characterize the phase changes with the propagation along the z -direction.

Now the total optical field \mathbf{E}, \mathbf{H} inside the coupler region is approximated by a linear combination of the modal basis fields (2.20) and (2.21) as

$$\begin{pmatrix} \mathbf{E} \\ \mathbf{H} \end{pmatrix}(x, z) = \sum_{v=b,s} \sum_{i=1}^{N_v} C_{vi}(z) \begin{pmatrix} \mathbf{E}_{vi} \\ \mathbf{H}_{vi} \end{pmatrix}(x, z), \quad (2.22)$$

with a priori unknown amplitudes C_{vi} that are allowed to vary with the propagation coordinate z . For ease of notation, these amplitudes are combined into amplitude vectors $\mathbf{C} = (\mathbf{C}_b, \mathbf{C}_s) = ((C_{bi}), (C_{si}))$. The governing equation for \mathbf{C} is derived using a variational principle. Unlike e.g. in Ref. [12], here no ‘phase matching’ arguments appear². Via the transformation $(r, \theta) \rightarrow (x, z)$, the tilt of the wave front of the bend modes (2.20) is explicitly taken into account.

2.4.1 Coupled mode equations

Consider the functional

$$\mathcal{F}(\mathbf{E}, \mathbf{H}) = \iint [(\nabla \times \mathbf{E}) \cdot \mathbf{H}^* - (\nabla \times \mathbf{H}) \cdot \mathbf{E}^* + i\omega\mu\mathbf{H} \cdot \mathbf{H}^* + i\omega\epsilon_0\epsilon\mathbf{E} \cdot \mathbf{E}^*] dx dz, \quad (2.23)$$

a 2-D restriction of the 3-D functional given in Ref. [15, Sec. 1.5.6, Eqn.(1.98)]. For the present 2-D setting, the above curl operators are interpreted with the convention of vanishing derivatives $\partial_y = 0$. The Maxwell equations $\nabla \times \mathbf{E} = -i\omega\mu\mathbf{H}$, and $\nabla \times \mathbf{H} = i\omega\epsilon_0\epsilon\mathbf{E}$ form a necessary condition for stationarity of \mathcal{F} with respect to variations of (\mathbf{E}, \mathbf{H}) .

By inserting the trial field (2.22) into the functional (2.23), we restrict \mathcal{F} to the fields allowed by the coupled mode ansatz. For the ‘optimal’ solution of the curl equations in the form of the field (2.22), the variation of $\mathcal{F}(\mathbf{C})$ is required to vanish for arbitrary variations $\delta\mathbf{C}$. Disregarding boundary terms, the first variations of \mathcal{F} at \mathbf{C} in the directions δC_{wj} , for $j=1, \dots, N_w$ and $w=b,s$, are

$$\delta\mathcal{F} = \int \sum_{v=b,s} \sum_{i=1}^{N_v} \left\{ M_{vi,wj} \frac{dC_{vi}}{dz} - F_{vi,wj} C_{vi} \right\} \delta C_{wj}^* dz - c.c. \quad (2.24)$$

where $c.c.$ indicates the complex conjugate of the preceding integrated term,

$$M_{vi,wj} = \int \mathbf{a}_z \cdot (\mathbf{E}_{vi} \times \mathbf{H}_{wj}^* + \mathbf{E}_{wj}^* \times \mathbf{H}_{vi}) dx, \quad (2.25)$$

$$F_{vi,wj} = -i\omega\epsilon_0 \int (\epsilon - \epsilon_v) \mathbf{E}_{vi} \cdot \mathbf{E}_{wj}^* dx, \quad (2.26)$$

² The arbitrariness in the choice of R renders the actual value of γ virtually meaningless [19]. Only the product γR is relevant.

and where \mathbf{a}_z is the unit vector in the z -direction. Consequently, one arrives at the coupled mode equations

$$\sum_{v=b,s} \sum_{i=1}^{N_v} M_{vi,wj} \frac{dC_{vi}}{dz} - \sum_{v=b,s} \sum_{i=1}^{N_v} F_{vi,wj} C_{vi} = 0, \text{ for } j = 1, \dots, N_w, \text{ and } w = b, s, \quad (2.27)$$

as a necessary condition for \mathcal{F} to become stationary for arbitrary variations δC_{wj} . The same expression is obtained from the complex conjugate part of (2.24). One can alternatively derive these coupled mode equations by means of a reciprocity identity [15, Sec. 4.3]. In matrix notation, (2.27) read

$$\mathbf{M}(z) \frac{d\mathbf{C}}{dz}(z) = \mathbf{F}(z) \mathbf{C}(z). \quad (2.28)$$

Due to the functional form of the bend modes and the varying distance between the bent and straight cores, the coefficients \mathbf{M} , \mathbf{F} are z -dependent. For explicit representations of these equations in the single mode case $N_b = N_s = 1$, see Ref. [8].

2.4.2 Coupler scattering matrices

In practice we solve the coupled mode equations numerically. The solution can be represented in terms of a transfer matrix \mathbf{T} (cf. Sec. 2.4.3) that relates the CMT amplitudes at the output plane $z = z_o$ to the amplitudes at the input plane $z = z_i$ of the coupler as

$$\mathbf{C}(z_o) = \mathbf{T} \mathbf{C}(z_i). \quad (2.29)$$

We still need to relate the transfer matrix, obtained directly as the solution of the coupled mode equations on the limited computational window, to the coupler scattering matrix as required for the abstract model of Sec. 2.2.

Outside the coupler region $[x_l, x_r] \times [z_i, z_o]$, it is assumed that the interaction between the fields associated with the bent waveguide and the straight waveguide is negligible. In this region, the individual modes propagating undisturbed with the harmonic dependences on the respective propagation coordinates are given by

$$\begin{aligned} a_p \begin{pmatrix} \tilde{\mathbf{E}}_{bp} \\ \tilde{\mathbf{H}}_{bp} \end{pmatrix} e^{-i\gamma_{bp}R(\theta-\theta_l)} \text{ for } \theta \leq \theta_l, & \quad A_q \begin{pmatrix} \tilde{\mathbf{E}}_{sq} \\ \tilde{\mathbf{H}}_{sq} \end{pmatrix} e^{-i\beta_{sq}(z-z_i)} \text{ for } z \leq z_i, \\ b_p \begin{pmatrix} \tilde{\mathbf{E}}_{bp} \\ \tilde{\mathbf{H}}_{bp} \end{pmatrix} e^{-i\gamma_{bp}R(\theta-\theta_o)} \text{ for } \theta \geq \theta_o, & \quad B_q \begin{pmatrix} \tilde{\mathbf{E}}_{sq} \\ \tilde{\mathbf{H}}_{sq} \end{pmatrix} e^{-i\beta_{sq}(z-z_o)} \text{ for } z \geq z_o \end{aligned} \quad (2.30)$$

Here a_p , A_q and b_p , B_q are the constant external mode amplitudes at the input and output ports of the coupler, as introduced in Sec. 2.2. The coordinate offsets z_i , θ_l and z_o , θ_o are as defined in Fig. 2.5.

Because of the assumption of vanishing external interaction, it is expected that outside the coupler the modes of straight waveguide propagate with constant am-

plitudes (with suitable phase changes). While the modes of the straight waveguide are typically well confined, the leaky bend modes may extend far beyond the bend waveguide, even reaching the region of the straight waveguide core. This affects intrinsically the way the CMT adjusts the amplitudes $C_s(z_o)$ in (2.29). The physical field around the exit planes of the CMT window consists of a superposition of the outgoing guided modes of the straight waveguide and a non-guided part due to the leaky bent modes. To extract the required external amplitudes A_q, B_q , we therefore project the total coupled field on the modes of the straight waveguide. Exploiting their orthogonality properties, the projection at the coupler output plane $z = z_o$ yields

$$B_q \exp(i\beta_{sq}z) = C_{sq} + \sum_{p=1}^{N_b} C_{bp} \frac{M_{bp,sq}}{M_{sq,sq}}, \quad (2.31)$$

where the mode overlaps $M_{mi,nj}$ occur already in the coupled mode equations (2.28). A similar procedure is applied to relate the coefficients A_q to the amplitudes C_{sq} at $z = z_i$. There is no need of such a projection for the external bend mode amplitudes, since the field strengths of the straight waveguide modes is usually negligible in the respective angular planes, where the major part of the bend mode profiles is located. Here merely factors are introduced to adjust for the offsets of the angular coordinates in (2.30).

Thus, given the solution (2.29) of the coupled mode equations in the form of the transfer matrix T , the scattering matrix S that relates the amplitudes a_p, b_p, A_q, B_q of the external fields as required in (2.6) is

$$S = QTP^{-1}, \quad (2.32)$$

where P and Q are $(N_b + N_s) \times (N_b + N_s)$ matrices with diagonal entries $P_{p,p} = \exp(-i\gamma_{bp}R\theta_i)$ and $Q_{p,p} = \exp(-i\gamma_{bp}R\theta_o)$, for $p = 1, \dots, N_b$, followed by the entries $P_{q+N_b, q+N_b} = \exp(-i\beta_{sq}z_i)$ and $Q_{q+N_b, q+N_b} = \exp(-i\beta_{sq}z_o)$, for $q = 1, \dots, N_s$. A lower left block is filled with elements $P_{q+N_b, p} = M_{bp,sq}/M_{sq,sq}|_{z=z_i}$ and $Q_{q+N_b, p} = M_{bp,sq}/M_{sq,sq}|_{z=z_o}$, for $q = 1, \dots, N_s$ and $p = 1, \dots, N_b$, respectively, that incorporate the projections. All other coefficients of P and Q are zero.

Indeed, as observed in Secs. 2.4.4 and 2.4.5, the projected amplitudes $|B_q|^2$ (or the related scattering matrix elements $|S_{sq,wj}|^2$) become stationary, when viewed as a function of the exit port position z_o , while at the same time the associated CMT solution $|C_{sq}(z)|^2$ (or the elements $|T_{sq,wj}|^2$ of the transfer matrix) exhibit an oscillatory behavior. Still, in the sense of the projections one can speak of ‘non-interacting, decoupled’ fields. This justifies the restriction of the computational window to z -intervals where the elements of S (not necessarily of T) attain constant absolute values around the input and output planes.

2.4.3 Remarks on the numerical procedures

Eq. (2.28) is solved numerically on a rectangular computational window $[x_l, x_r] \times [z_i, z_o]$ as shown in Fig. 2.5. For given z , the integrals (2.25) and (2.26) are numerically computed by the trapezoidal rule [46] using a uniform discretization of $[x_l, x_r]$ into intervals of length h_x .

Subsequently, a standard fourth order Runge-Kutta scheme [46] is applied to solve the coupled mode equations over the computational domain $[z_i, z_o]$, which is split into intervals of equal length h_z . Exploiting the linearity of (2.28), the procedure is formulated directly for the transfer matrix \mathbf{T} , which gives

$$\frac{d\mathbf{T}}{dz}(z) = \mathbf{M}(z)^{-1} \mathbf{F}(z) \mathbf{T}(z) \quad (2.33)$$

with initial condition $\mathbf{T}(z_i) = \mathbf{I}$, where \mathbf{I} is the identity matrix, such that $\mathbf{C}(z) = \mathbf{T}(z) \mathbf{C}(z_i)$. While the evaluation of the resonator properties via (2.32) and (2.8), (2.9) requires only the solution $\mathbf{T} = \mathbf{T}(z_o)$ at the coupler output plane $z = z_o$, examination of the evolutions of $\mathbf{T}(z)$ and $\mathbf{S}(z)$ turns out to be instructive.

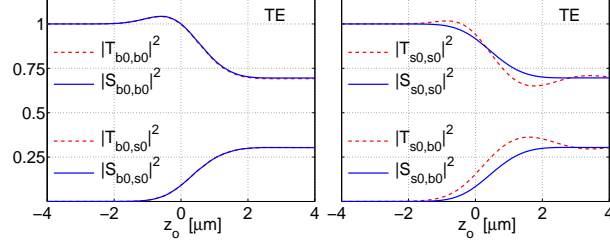
2.4.4 Couplers with monomodal bent waveguide

Consider bent-straight waveguide couplers formed by straight and circularly bent cores of widths $w_s = 0.4 \mu\text{m}$ and $w_c = 0.5 \mu\text{m}$ with refractive index $n_c = n_s = 1.5$, embedded in a background with refractive index $n_b = 1$. The bend radius R and the distance g between the cores are varied. The CMT simulations are carried out on a computational window of $[x_l, x_r] \times [z_i, z_o] = [0, R + 10] \mu\text{m} \times [-R + 1, R - 1] \mu\text{m}$, if $R \leq 5 \mu\text{m}$, otherwise on a window of $[x_l, x_r] \times [z_i, z_o] = [R - 5, R + 10] \mu\text{m} \times [-8, 8] \mu\text{m}$, discretized with step sizes of $h_x = 0.005 \mu\text{m}$ and $h_z = 0.1 \mu\text{m}$.

First we look at the interaction of waves for vacuum wavelength $\lambda = 1.05 \mu\text{m}$ and bend radius $R = 5 \mu\text{m}$. For this setting both constituent waveguides are single modal, with propagation constants $\gamma/k = 1.29297 - i7.5205 \cdot 10^{-6}$ for the TE_0 bend mode, and $\beta/k = 1.3137$ for the straight waveguide. The CMT analysis generates 2×2 transfer matrices \mathbf{T} and scattering matrices \mathbf{S} that can be viewed as being z -dependent in the sense as discussed for 2.33. Fig. 2.6 shows the evolution of the matrix elements with the position $z = z_o$ of the coupler output plane.

The matrix elements $T_{o,i}$ and $S_{o,i}$ relate the amplitudes of an input mode i to an output mode o . Thus for the present normalized modes the absolute squares can be viewed as the relative fractions of optical power transferred from mode i at the input plane $z = z_i$ to mode o at the output plane $z = z_o$. After an initial interval, where these quantities remain stationary, one observes variations around the central plane $z = 0$, which correspond to the interaction of the waves. Here the mutually nonorthogonal basis fields are strongly overlapping; it is therefore not surprising that the levels of specific components of $|T_{o,i}|^2$ and $|S_{o,i}|^2$ exceed 1 in this interval.

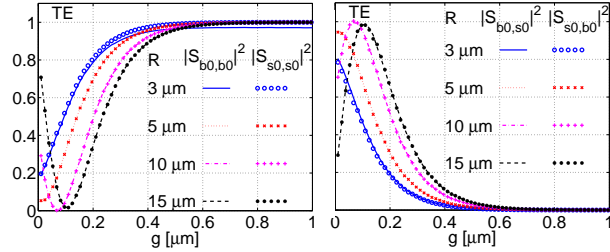
Fig. 2.6 Elements of the TE transfer matrix \mathbf{T} and scattering matrix \mathbf{S} as a function of the output plane position z_o , for couplers as introduced in Sec. 2.4.4 with $R = 5\mu\text{m}$ and $g = 0.2\mu\text{m}$, at $\lambda = 1.05\mu\text{m}$ (Illustrations taken from Ref. [17]).



After the region of strongest interaction, near the end of the z -computational interval, one finds that the elements $|T_{b0,i}|^2$ that map to the bend mode amplitude become stationary again, while the elements $|T_{s0,i}|^2$ related to the output to the straight mode still show an oscillatory behavior. This is due to the interference effects as explained in Sec. 2.4.2. The proper amplitudes of the modes of the bus channel can be extracted by applying the projection operation (2.31); the corresponding matrix elements $|S_{s0,i}|^2$ attain stationary values, such that the ‘coupling strength’ predicted for the involved modes does not depend on the position of the coupler output plane.

The final scattering matrix \mathbf{S} that enters the relations (2.8) and (2.9) should be considered a static quantity, computed for the fixed computational interval $[z_i, z_o]$. From the design point of view, one is interested in the elements of this matrix (the ‘coupling coefficients’) as a function of the resonator / coupler design parameters. Fig. 2.7 summarizes the variation of \mathbf{S} with the width of the coupler gap, for a series of different bend radii.

Fig. 2.7 Scattering matrix elements $|S_{o,i}|^2$ versus the gap width g , for couplers as considered in Sec. 2.4.4 with cavity radii $R = 3, 5, 10, 15\mu\text{m}$, for TE polarized waves at $\lambda = 1.05\mu\text{m}$ (Illustrations taken from Ref. [17]).



For all radii, one observes that for large gap widths, the non-interacting fields lead to curves that are constant at levels of unity for $|S_{s0,s0}|^2$ (full transmission along the straight waveguide), moderately below unity for $|S_{b0,b0}|^2$ (due to the attenuation of the isolated bend mode), and zero for $|S_{b0,s0}|^2$ and $|S_{s0,b0}|^2$ (decoupled fields). As the gap width decreases, the growing interaction between the modes in the two cores increases the cross coupling $|S_{b0,s0}|^2$, $|S_{s0,b0}|^2$ and decreases the self coupling $|S_{s0,s0}|^2$, $|S_{b0,b0}|^2$. This continues until a maximum level of power transfer is attained (where the level should depend on the ‘phase mismatch’ between the basis fields, though a highly questionable notion in case of the bend modes [19]). If the gap is

further reduced, the cross coupling coefficients decrease, even if the strength of the interaction is increased. This is due to ‘forth and back coupling’, where along the propagation axis a major part of the optical power is first transferred completely from the input channel to the adjacent waveguide, then back to the input core [47]. Therefore one should distinguish clearly between the magnitudes of the coefficients (2.26) in the differential equations that govern the coupling process, and the solution of these equations for a finite interval, the net effect of the coupler, represented by the scattering matrix \mathbf{S} .

For the symmetric computational setting used for the simulations in Figs. 2.6 and 2.7, the reciprocity requirement, i.e. the symmetry of \mathbf{S} (see Sec. 2.2) is satisfied appropriately. In Fig. 2.6, the curves related to $|S_{s0,b0}|^2$ and $|S_{b0,s0}|^2$ end in nearly the same level at $z = z_0$. One observes some deviations for configurations with very small bend radii and gaps close to zero. For such extreme cases, the underlying ansatz (2.22) of CMT may not be valid. Otherwise the symmetry of the scattering matrices provides a useful means to assess the accuracy of the CMT simulations, beyond merely the power balance constraint.

2.4.5 Couplers with multimodal cavity segments

Next we consider couplers that consist of a straight waveguide close to a single bent interface that supports a range of WGMs. A parameter set similar to Sec. 2.4.4 is adopted, with $n_c = n_s = 1.5$, $n_b = 1.0$, $R = 5 \mu\text{m}$, $w_s = 0.4 \mu\text{m}$, and $g = 0.2 \mu\text{m}$, for a reference wavelength $\lambda = 1.05 \mu\text{m}$. A few WGMs supported by the curved interface are illustrated in Fig. 2.4. The CMT analysis is carried out on a computational window $[x_l, x_r] = [0, 15] \mu\text{m}$, $[z_l, z_o] = [-4, 4] \mu\text{m}$ with large extent in the (radial) x -direction, in order to capture the radiative parts of the lossy higher order bend fields. Step sizes for the numerical integrations are $h_x = 0.005 \mu\text{m}$, $h_z = 0.1 \mu\text{m}$, as before.

It is not a priori evident how many basis fields are required for a particular simulation. Fig. 2.8 shows the effect of the inclusion of the higher order WGMs on the evolution of the primary coefficients of the matrix \mathbf{S} . The self coupling coefficient $|S_{b0,b0}|^2$ of the fundamental bend field is hardly influenced at all, and there is only a minor effect on the cross coupling coefficients $|S_{s0,b0}|^2$ and $|S_{b0,s0}|^2$. But the self coupling coefficient $|S_{s0,s0}|^2$ of the straight mode is reduced by a substantial amount with the inclusion of the first order bend mode, due to the additional coupling to that basis field. Apparently, for the present structure it is sufficient to take just the two or three lowest order bend modes into account. This is one of the advantages of the CMT approach, where one can precisely analyze the significance of the individual basis modes (cf. the comments in Sec. 2.6.2).

With three cavity fields and the mode of the straight waveguide, the CMT simulations lead to 4×4 coupler transfer and scattering matrices. The evolution of the 16 matrix elements follows similar qualitative trends as in Fig. 2.6, albeit with additional intricacy due to the multimodal cavity [17]. It turns out that, for the present case, the coupling between the bend modes themselves is practically negligible. Ac-

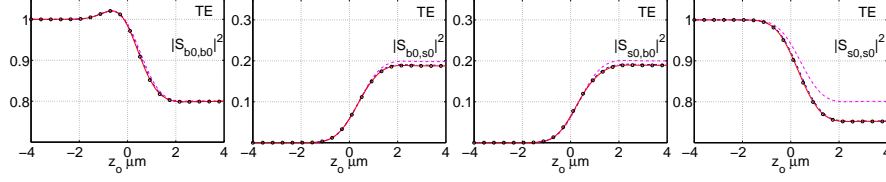


Fig. 2.8 Effect of the inclusion of higher order bend modes on the evolution of the scattering matrix for the multimode coupler of Sec. 2.4.5. Results for TE waves with one (dashed line), two (dash-dotted line), three (solid line), and four cavity modes (dotted line) taken into account (Illustrations taken from Ref. [17]).

cording to Fig. 2.9, the elements of the scattering matrix exhibit a similar variation with the gap width as found for the former monomode couplers (cf. Fig. 2.7). With growing separation the cross coupling coefficients tend to zero. The constant levels attained by the self coupling coefficients of the bend modes are determined by the power the respective mode loses in traversing the computational window. Also here, with the exception of configurations with almost closed gap, we see in the central and right plots that the cross coupling coefficients with reversed indices coincide, i.e. the simulations obey reciprocity.

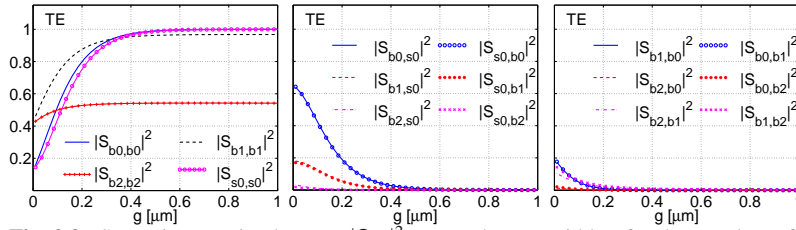


Fig. 2.9 Scattering matrix elements $|S_{oi}|^2$ versus the gap width g for the couplers of Sec. 2.4.5. The CMT simulations are based on three WGMs (indices b0, b1, b2) and on the field of the straight waveguide (index s0) (Illustrations taken from Ref. [17]).

2.5 Spectrum evaluation

Having access to the bend mode propagation constants and the coupler scattering matrices, (2.8) permit to compute the resonator response. This can be done in several ways with adequate efficiency.

- *Direct method*: In principle the spectral response can be obtained by repeating all calculations for a series of wavelengths. This requires recalculating the bend mode propagation constants and scattering matrices.
- *Interpolation of reduced scattering matrices*: A substantial computational overhead can be avoided, if one calculates the relevant quantities merely for a few distant wavelengths, and then interpolates between these values. The interpola-

tion procedure, however, should be applied to quantities that vary slowly with the wavelength.

In line with the reasoning at the end of Sec. 2.2.1, one expects that the wavelength dependence of the transmission is determined mainly by the phase gain along the cavity, which is caused by a comparably slow wavelength dependence of the bend mode propagation constants γ_{bp} , but multiplied by the cavity lengths L, \tilde{L} . If a substantial part of the cavity is already covered by the couplers, then the matrices \mathbf{S} exhibit fast phase oscillations with the wavelength, such that \mathbf{S} is not directly suitable for interpolation [47]. The coupled wave interaction might introduce additional slow wavelength dependence.

To separate the two scales in \mathbf{S} , divide by the exponentials that correspond to the undisturbed wave propagation. This gives the reduced scattering matrix

$$\mathbf{S}' = \mathbf{Q}^0 \mathbf{S} (\mathbf{P}^0)^{-1}. \quad (2.34)$$

Here \mathbf{P}^0 and \mathbf{Q}^0 are diagonal matrices with entries $P_{j,j}^0$ and $Q_{j,j}^0$ as defined for \mathbf{P} and \mathbf{Q} in (2.32). Formally, one can view \mathbf{S}' as the scattering matrix of a coupler with zero length, where the interaction takes place instantaneously at $z = 0$. This modification of \mathbf{S} , applied analogously to $\tilde{\mathbf{S}}$, is compensated by redefining the lengths of the external cavity segments as $L' = \tilde{L}' = \pi R$, by changing the matrices \mathbf{G} and $\tilde{\mathbf{G}}$ accordingly, and, where necessary, by taking into account the altered phase relations on the external straight segments.

After these modifications, the new matrices \mathbf{G}' and $\tilde{\mathbf{G}}'$ capture the phase gains of the cavity fields along the full circumference. These show only slow wavelength dependence, just as \mathbf{S}' and $\tilde{\mathbf{S}}'$, such that they can be successfully interpolated [47].

- *Assumption of a constant scattering matrix:* As an extreme variant of the former approximation, (2.8) are evaluated with the scattering matrix for a central reference wavelength, together with rigorously computed or interpolated cavity mode propagation constants.

2.6 Circular microresonators in two spatial dimensions

The ingredients discussed so far are now combined into a simulation tool for entire resonator structures. We compare the results of the CMT approach with finite-difference-time-domain (FDTD) simulations based on a second order Yee mesh with total field/scattered field formulation and artificial transparent (perfectly matched layer, PML) boundary conditions [17, 48]. While the present examples consider exclusively TE polarized fields, the abstract reasoning in Sec. 2.2 and the CMT formalism in Sec. 2.4 are just as well applicable for TM polarization [17].

2.6.1 Microring

We consider the symmetric ring resonator with monomode cavity made up of the couplers of Sec. 2.4.4. In line with the assumptions leading to (2.8) and (2.9), the fundamental mode of the bus waveguides is launched at the input port with unit power, with no incoming field at the add port. Fig. 2.10 shows the spectral response for parameters $n_c = n_s = 1.5$, $n_b = 1.0$, $w_c = 0.5 \mu\text{m}$, $w_s = 0.4 \mu\text{m}$, $R = 5 \mu\text{m}$, $g = \tilde{g} = 0.2 \mu\text{m}$, in a wavelength interval around the former arbitrarily chosen design wavelength $\lambda = 1.05 \mu\text{m}$. The further computational setting is as given for Fig. 2.6.

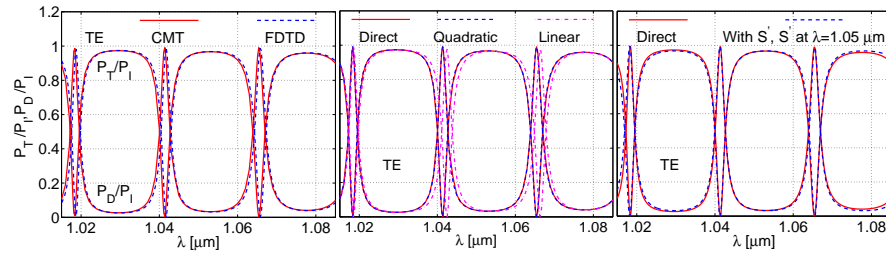


Fig. 2.10 Relative transmitted power P_T and dropped power P_D versus the wavelength for a ring resonator as discussed in Sec. 2.6.1; Left: CMT and FDTD results. Center: CMT results with spectrum evaluation by the direct and by the interpolation method with nodal wavelengths $1.015 \mu\text{m}$ and $1.085 \mu\text{m}$ (linear), or $1.015 \mu\text{m}$, $1.05 \mu\text{m}$, and $1.085 \mu\text{m}$ (quadratic interpolation). Right: Spectrum evaluation by the direct and the constant scattering matrix method (Illustrations taken from Ref. [17]).

One observes the familiar ring resonator resonance pattern with dips in the transmitted power and peaks in the dropped intensity. According to Fig. 2.7, the present parameter set specifies configurations with rather strong interaction in the coupler regions ($|S_{b0,s0}|^2 = 30\%$), such that the resonances are relatively wide, with a substantial amount of optical power being directly transferred to the drop port also in off-resonant states.

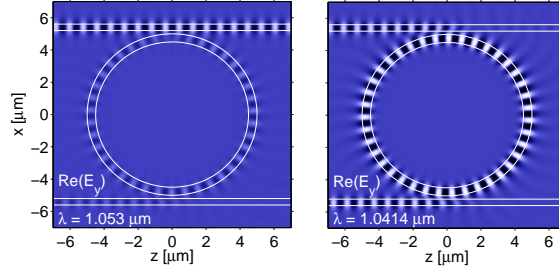
The CMT results are compared with FDTD simulations (for numerical details, see Ref. [17]). As seen in the left plot of Fig. 2.10, we find an excellent agreement between the CMT and the FDTD results for TE polarization (though one observes minor deviations for the TM case, where the fields are discontinuous [17]). Even in the present 2-D setting, these FDTD calculations typically require a computation time of several hours, while the CMT analysis (with interpolation) delivers the entire spectrum in just a few minutes.

The central plot of Fig. 2.10 shows the resonator spectrum as obtained by interpolating bend mode propagation constants and CMT scattering matrices for only two (linear interpolation) or three (quadratic interpolation) distinct wavelengths, according to Sec. 2.5. While small deviations remain for the linear approximation, on the scale of the figure the curves related to quadratic interpolation are hardly distinguishable from the direct CMT results. The right-most plot of Fig. 2.10 shows

that the assumption of a constant scattering matrix is perfectly reasonable for the current setting. Minor deviations appear only far from the reference wavelength. Thus the interpolation approach provides a very effective means to predict accurately the resonator spectrum, in particular if narrow dips / peaks in the responses of high-quality resonators have to be resolved, such that the direct evaluation would be computationally expensive. We shall exploit this later on for the 3-D simulations.

The principal field components for off-resonance and resonant configurations are illustrated in Fig. 2.11. In the off-resonance state one observes the large through transmission and small amplitudes of the waves in the drop-port along with minor wave amplitudes in the cavity. At the resonances, the straight transmission is almost suppressed. A major part of the input power arrives at the drop-port, and the leaky nature of the ring mode can be clearly observed.

Fig. 2.11 CMT results for the microring structure of Fig. 2.10. Snapshots of the principal components of the physical TE field, off-resonance (first plot) and at resonance (second plot). For visualization purposes the coupler computational window has been extended to $[z_1, z_0] = [-4, 8] \mu\text{m}$ (Illustrations taken from Ref. [17]).



2.6.2 Microdisk

Here we look at the symmetrical microdisk resonator that is constituted by two of the multimode couplers of Sec. 2.4.5. The computational setting and all parameters are identical to the data given in Sec. 2.4.5, for gap widths $g = \tilde{g} = 0.2 \mu\text{m}$. First consider the spectral response obtained by CMT computations, where besides the mode of the straight waveguide, different sets of WGMs are used as basis fields. The curves in the left plot of Fig. 2.12 exhibit only specific extrema from the full spectrum with similar extremum levels. Hence these resonances can clearly be assigned to the respective TE_0 or TE_1 WGM. As these modes circulate along the cavity with different propagation constants, individual resonance conditions are satisfied in general at different wavelengths. TE_2 plays obviously only an inconsequential role.

The effect of the inclusion of higher order WGMs on the resonator response is shown in the right plot of Fig. 2.12. While the fundamental and first order WGMs are essential for the present resonator, inclusion of the second order WGM into the CMT analysis leads only to minor changes. Thus for this microdisk configuration, it is sufficient to take into account the two lowest order cavity modes as basis fields to predict reliably the spectral response. This was already evident in the coupler

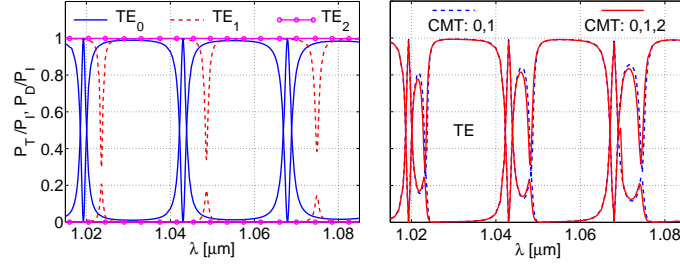


Fig. 2.12 TE power spectrum of the microdisk resonator of Sec. 2.6.2. CMT analysis with different sets of basis modes. Besides the mode of the straight waveguide, only one WGM (TE_0 , TE_1 , or TE_2 ; left), or the two and three lowest order WGMs (right) is/are taken into account (Illustrations taken from Ref. [17]).

analysis of Fig. 2.8. Due to negligible interaction among the cavity modes themselves (which might be caused by the presence of the couplers, i.e. the perturbation through the bus waveguides), the resonance locations in the combined CMT analysis (right plot) coincide well with those predicted by the single mode calculation (left plot). Similar conclusions can be drawn by inspection of the local mode amplitudes $\mathbf{b} = (b_q)$, as functions of the wavelength, that are predicted by the CMT model [17].

The comparison of CMT and FDTD spectra in Fig. 2.13 shows a quite satisfactory agreement. The right plot validates the interpolation approach of Sec. 2.5. As before, we see that the quadratic interpolation of the scattering matrix coefficients and propagation constants leads to curves that are almost indistinguishable from the directly computed results.

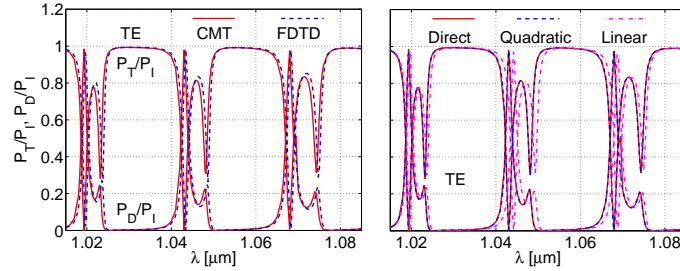


Fig. 2.13 Power transmission through the microdisk resonator of Sec. 2.6.2. Left: CMT and FDTD spectra for TE modes. Right: CMT spectra (four basis modes) computed directly, and by interpolation of data evaluated at the nodal wavelengths $1.015\ \mu\text{m}$, $1.085\ \mu\text{m}$ (linear) and $1.015\ \mu\text{m}$, $1.05\ \mu\text{m}$, $1.085\ \mu\text{m}$ (quadratic interpolation) (Illustrations taken from Ref. [17]).

Fig. 2.14 shows examples for the corresponding field distributions. Off-resonance, most of the input power is directly transferred to the through-port. At the wavelength corresponding to one of the minor resonances, the field pattern in the cavity exhibits a nearly circular nodal line corresponding to the radial minimum in the profile of the first order WGM (cf. Fig. 2.4). As seen in Fig. 2.13, here the first order mode

carries most of the power inside the cavity. The deviation from the circular pattern is caused by the interference with the fundamental WGM, which is also excited at this wavelength with a small power fraction. The major resonance related to the fundamental mode is of higher quality, with much larger intensity in the cavity, almost full suppression of the waves in the through-port and nearly complete drop of the input power.

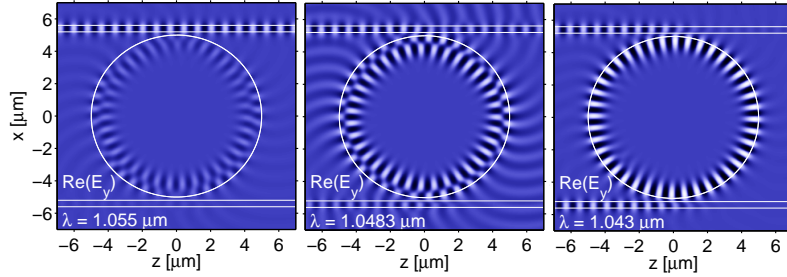


Fig. 2.14 Snapshots of the real physical electric field for the microdisk resonator of Sec. 2.6.2; CMT simulations with four basis modes. The wavelengths correspond to an off-resonance state (left), and to minor (center) and major resonances (right). The gray scale levels of the plots are comparable (Illustration taken from Ref. [17]).

2.7 Circular optical microresonators in 3-D

So far we restricted ourselves to two spatial dimensions, in order to explain concepts and phenomena behind the CMT model, and for purposes of rigorous numerical assessment. There are practical circumstances, however, where the 2-D setting is definitely inadequate. e.g. when an effective index approximation seems not reasonable, when the assumption of decoupled polarizations appears to be inappropriate, when the vectorial nature of the fields might be important (as in the case of cavity or bus cores with pronouncedly hybrid modes), or the obvious case of vertically coupled microresonators. One then has to resort to fully 3-D simulations. The abstract resonator model in Sec. 2.2 remains applicable, irrespectively of the number of spatial dimensions. With the exception of an additional integration along the third, vertical y -axis, the CMT formalism for the couplers is essentially identical to what has been discussed in Sec. 2.4. Thus the extension of the present CMT resonator model to 3-D [18] should be straightforward, in principle.

The real additional complexity is the task of generating the required basis fields. Analytic solutions, as in 2-D, for modes of straight and — especially — bent waveguides in 3-D, i.e. with 2-D cross sections, do not exist; numerical mode solvers have to be applied. For the simulations discussed in this section we could rely on a semi-analytical technique based on film mode matching (FMM) [20, 49, 50]. The modal eigenvalue problem is addressed by dividing the waveguide cross section

plane into vertical slices such that the permittivity profile is constant along the horizontal/radial axis. On each slice the modal field is expanded rigorously into eigenfunctions (modes of 1D multilayer slab waveguides) associated with the local refractive index profile, where the sets of eigenfunctions are discretized by Dirichlet boundary conditions sufficiently far above and below the interesting region around the waveguide core. 3-D modes are obtained by connecting the expansions on the individual slices such that the full field satisfies all continuity requirements at the vertical interfaces, and shows the appropriate behavior in the outermost regions. The rigorous mode profile approximations are represented quasi-analytically, which proves to be advantageous for the subsequent use as basis fields within the CMT formalism (integrations).

For the 3-D coupler introduced in Fig. 2.15(a), the coupled field ansatz (2.22) applies, with an additional nontrivial dependence on the vertical y -axis, introduced by the — now truly vectorial — mode profiles (2.21) and (2.20) of the straight and bent cores. The functional (2.23) and consequently the matrix elements (2.25), (2.26) receive an additional y -integration. Otherwise the reasoning of Secs. 2.4.1, 2.4.2, and 2.4.3 remains valid.

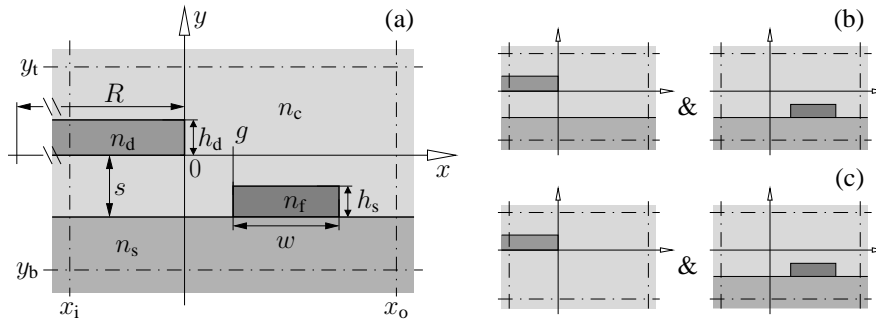


Fig. 2.15 (a): Coupler setting in 3-D, a cross section perpendicular to the direction of propagation at $z = 0$. A disk cavity of radius R , core refractive index n_d and height h_d is coupled to bus waveguides of core refractive index n_f , width w and height h_s . Here the disk and the bus waveguide are placed at different levels, at a vertical distance s and at a horizontal position g . Negative values for g represent overlapping components. n_s and n_c are the refractive indices of the substrate and cladding regions. (b) and (c): Choices for constituting structures for the CMT analysis. In (b) the substrate is included into the cavity mode analysis, whereas it is excluded in (c) (Illustrations taken from Ref. [18]).

One should be aware that the choice of the constituting structures, i.e. of the refractive index profiles for which the basis modes are calculated, is not at all unique. For the structure of Fig. 2.15(a), for example, the substrate could be included into the computation of the cavity mode (b), or omitted (c). In the first case the permittivity profile ϵ_b of the cavity is closer to the true permittivity ϵ of the full coupler. Hence their difference, i.e. the perturbation in (2.26), is small, and one can expect a better overall approximation. Option (b) also allows to take the influence of the substrate

on the cavity modes into account. As an added benefit, the integrals (2.26) in the coupled mode equations extend only over the disk and the straight waveguide cores, not over the substrate domain. As a disadvantage, one has to recalculate the cavity modes for different vertical separations s . This can be avoided in the setting (c) of Fig. 2.15. In general, the choice of the constituting structures and the selection of the basis fields is a matter of physical intuition and of convenience for the subsequent numerics. For the present configuration with low to moderate index contrast between substrate and cladding, we observed hardly any difference [18].

The performance of the coupler of Fig. 2.15 is affected by both the vertical separation s and the relative horizontal core position g . Their influence on the elements of the coupler scattering matrix is shown in Fig. 2.16. While a rigorous explanation of these variations on the basis of modal interaction strengths, as in the 2-D case, turns out to be difficult, the qualitative behavior can still be understood. For large horizontal separations g , due to less mode interaction, all self coupling coefficients (a), (d) tend to 1, and the cross coupling coefficients (b), (c), (e), (f) vanish. Also, the cross coupling coefficients satisfy the self consistency requirement of reciprocity. A reduction of the vertical separation ((a), (b), (c) vs. (d), (e), (f)) increases the strength of the interaction. For the small vertical distance, also the interaction (f) between the cavity modes, affected by the presence of the straight core, is clearly no longer negligible. Comparisons, as far as possible, of these CMT results with simulations by a beam propagation method show a reasonable agreement [18].

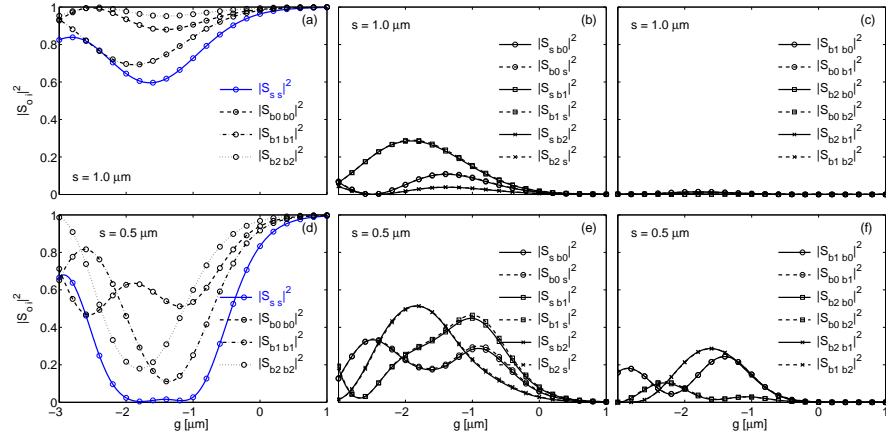


Fig. 2.16 Scattering matrix elements of the 3-D couplers of Fig. 2.15 versus the relative horizontal core position g , for different vertical separations s . The CMT computation is based on the single mode of the straight core (index s), together with the first three lowest order modes (b_0 , b_1 , b_2) of the disk cavity. (a, d): self coupling coefficients; (b, e): cross coupling straight/bent core; (c, f): cross coupling between bend modes. The coupler consist of a straight waveguide with $w = 2.0\mu\text{m}$, $h_s = 0.140\mu\text{m}$, $n_f = 1.98$, $n_s = 1.45$, $n_c = 1.4017$, and a disk cavity with $n_d = 1.6062$, $h_d = 1.0\mu\text{m}$, $R = 100\mu\text{m}$ (Illustrations taken from Ref. [18]).

The resultant effect of the relative vertical and horizontal core positions on the spectral response of the full 3-D vertically coupled microdisk-resonator is depicted in Fig. 2.17. The data is computed with a constant scattering matrix at the reference wavelength $\lambda = 1.55 \mu\text{m}$ [18] (cf. Sec. 2.5). For configuration (a) with moderate interaction strength, one observes a set of three resonances that appear periodically, each corresponding to one of the three low loss cavity modes involved. Reducing either the horizontal separation (b) or the vertical distance (c) leads to much stronger coupling with deteriorated resonances. The resonance characteristics disappear altogether in the somewhat extreme situation (d).

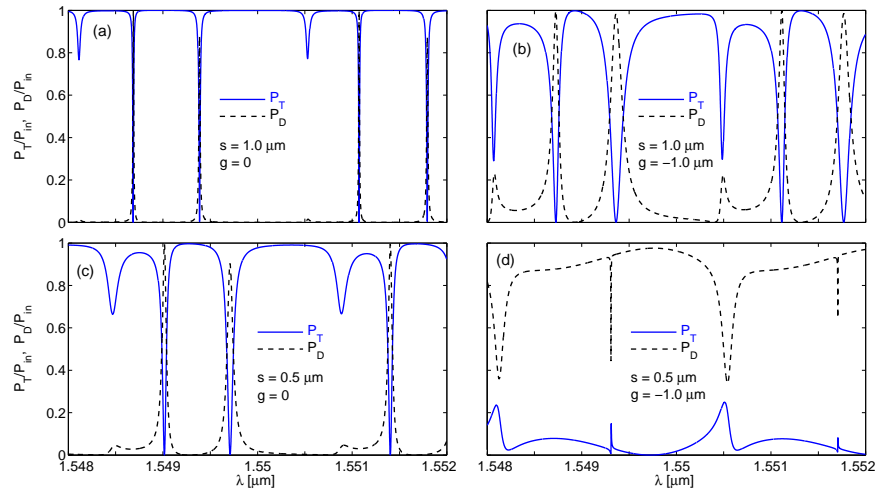


Fig. 2.17 Spectral response of the vertically coupled microdisk resonator consisting of two identical couplers as in Fig. 2.16 with different vertical separations s , and horizontal positioning g (Illustrations taken from Ref. [18]).

2.8 Concluding remarks

The ab-initio frequency domain model, as discussed in this chapter, originates from the physical notions that are commonly used to describe the functioning of circular microresonators. Bend modes supported by the segments of the ring or disk-shaped cavities, together with modal fields of the straight bus cores, constitute the basis for the quantitative coupled-mode-theory of the evanescent wave interaction in the coupler regions.

For the present frequency domain description, it is straightforward to take into account material dispersion. Since the spectral response is evaluated as a scan over vacuum wavelengths, the quantities that enter the CMT equations can be determined

directly for the material properties at the respective wavelengths. The remarks from Sec. 2.5 on interpolation schemes for efficient spectrum evaluation apply as well.

Unlike with other common, purely numerical methods, here we have convenient access to all local modal amplitudes, which allows characterizing and analyzing the resonances. One observes that, for most reasonable configurations, only one or a few cavity modes play a significant role. It is then possible to accurately predict the spectral response of the device in question by very efficient, quasi-analytical calculations. Our thorough study of the 2-D version of the model serves to explain all concepts; the examples permit a thorough benchmarking versus rigorous finite-difference time-domain calculations. Extension of the formalism to realistic resonators in 3-D is straightforward. Here in particular the computational advantages of the CMT approach are revealed, since hardly any other, even moderately efficient simulation tool is available for practical design work.

Beyond the vertically coupled micro-disk resonator of Sec. 2.7, the approach has shown to be sufficiently flexible to handle also quite exotic 3-D configurations, like the device with hybrid ring cavity and pedestal waveguides of Ref. [18]. Finally, the CMT model is ideally suited to incorporate small changes in the configuration, e.g. for purposes of the evaluation of fabrication tolerances, or for predicting the effects of tuning mechanisms [8, 51].

Acknowledgements This work was carried out as a part of the project ‘NAIS’ (IST-2000-28018), funded by the European Commission. K. R. Hiremath also acknowledges support by the DFG (German Research Council) Research Training Group ‘Analysis, Simulation and Design of Nanotechnological Processes’, University of Karlsruhe. The authors thank R. Stoffer for his hard work on the 3-D simulations. They are grateful to H. J. W. M. Hoekstra, E. van Groesen, and their colleagues in the NAIS project for many fruitful discussions.

References

1. Vahala, K.: *Optical Microcavities*. World Scientific (2004)
2. Michelotti, F., Driessen, A., et al., editors: *Microresonators as building blocks for VLSI photonics*, volume 709 of *AIP conference proceedings* (2004)
3. Heebner, J., Grover, R., et al.: *Optical Micro-Resonators: Theory, Fabrication, and Applications*. Springer (2007)
4. Landobasa, Y. M., Darmawan, S., et al.: Matrix analysis of 2-D microresonator lattice optical filters. *IEEE J. Quantum Electron.* **41**, 1410–1418 (2005)
5. Popović, M. A., Manolatu, C., et al.: Coupling-induced resonance frequency shifts in coupled dielectric multi-cavity filters. *Opt. Express* **14**, 1208–1222 (2006)
6. Stokes, L. F., Chodorow, M., et al.: All single mode fiber resonator. *Opt. Lett.* **7**, 288–290 (1982)
7. Yariv, A.: Universal relations for coupling of optical power between microresonators and dielectric waveguides. *IEEE Electron. Lett.* **36**, 321–322 (2000)
8. Hammer, M., Hiremath, K. R., et al.: Analytical approaches to the description of optical microresonator devices. In Michelotti, F., Driessen, A., et al., editors, *Microresonators as building blocks for VLSI photonics*, volume 709 of *AIP conference proceedings*, 48–71 (2004)
9. Okamoto, K.: *Fundamentals of Optical Waveguides*. Academic Press, U.S.A (2000)

10. Klunder, D. J. W., Krioukov, E., et al.: Vertically and laterally waveguide-coupled cylindrical microresonators in Si_3N_4 on SiO_2 technology. *Appl. Phys. B*, **73**, 603–608 (2001)
11. Klunder, D. J. W., Balistreri, M. L. M., et al.: Detailed analysis of the intracavity phenomena inside a cylindrical microresonator. *IEEE J. Lightw. Technol.* **20**, 519–529 (2002)
12. Rowland, D. R., Love, J. D.: Evanescent wave coupling of whispering gallery modes of a dielectric cylinder. *IEEE Proc.: Optoelectron.* **140**, 177–188 (1993)
13. Chin, M. K., Ho, S. T.: Design and modeling of waveguide coupled single mode microring resonator. *IEEE J. Lightw. Technol.* **16**, 1433–1446 (1998)
14. Cusmai, G., Morichetti, F., et al.: Circuit-oriented modelling of ring-resonators. *Opt. Quantum Electron.* **37**, 343–358 (2005)
15. Vassallo, C.: *Optical Waveguide Concepts*. Elsevier, Amsterdam (1991)
16. Hall, D. G., Thompson, B. J., editors: *Selected Papers on Coupled-Mode Theory in Guided-Wave Optics*, volume MS 84 of *SPIE Milestone Series*. SPIE Optical Engineering Press, Bellingham, Washington USA (1993)
17. Hiremath, K. R., Stoffer, R., et al.: Modeling of circular integrated optical microresonators by 2-D frequency domain coupled mode theory. *Opt. Commun.* **257**, 277–297 (2006)
18. Stoffer, R., Hiremath, K. R., et al.: Cylindrical integrated optical microresonators: Modeling by 3-D vectorial coupled mode theory. *Opt. Commun.* **256**, 46–67 (2005)
19. Hiremath, K. R., Hammer, M., et al.: Analytic approach to dielectric optical bent slab waveguides. *Opt. Quantum Electron.* **37**, 37–61 (2005)
20. Prkna, L., Hubálek, M., et al.: Field modeling of circular microresonators by film mode matching. *IEEE J. Sel. Top. Quantum Electron.* **11**, 217–223 (2005)
21. Stoffer, R., Hiremath, K. R., et al.: Comparison of coupled mode theory and FDTD simulations of coupling between bent and straight optical waveguides. In Michelotti, F., Driessen, A., et al., editors, *Microresonators as building blocks for VLSI photonics*, volume 709 of *AIP conference proceedings*, 366–377 (2004)
22. Van, V., Absil, P., et al.: Propagation loss in single-mode GaAs-AlGaAs microring resonators: measurement and model. *IEEE J. Lightw. Technol.* **19**, 1734–1739 (2001)
23. Absil, P. P., Hryniewicz, J. V., et al.: Compact microring notch filters. *IEEE Photonics Technol. Lett.* **14**, 398–400 (2000)
24. Chu, S. T., Little, B. E., et al.: Cascaded microring resonators for crosstalk reduction and spectrum cleanup in add-drop filters. *IEEE Photonics Technol. Lett.* **11**, 1423–1425 (1999)
25. Yariv, A., Xu, Y., et al.: Coupled-resonator optical waveguide: a proposal and analysis. *Opt. Lett.* **24**, 711–713 (1999)
26. Little, B. E., Chu, S. T., et al.: Microring resonator channel dropping filters. *IEEE J. Lightw. Technol.* **15**, 998–1005 (1997)
27. Grover, R., Van, V., et al.: Parallel-cascaded semiconductor microring resonators for high-order and wide-FSR filters. *IEEE J. Lightw. Technol.* **20**, 900–905 (2002)
28. Hryniewicz, J. V., Absil, P. P., et al.: Higher order filter response in coupled microring resonators. *IEEE Photonics Technol. Lett.* **12**, 320–322 (2000)
29. Chu, S. T., Little, B. E., et al.: An eight-channel add-drop filter using vertically coupled microring resonators over a cross grid. *IEEE Photonics Technol. Lett.* **11**, 691–693 (1999)
30. Little, B. E., Chu, S. T., et al.: Microring resonator arrays for VLSI photonics. *IEEE Photonics Technol. Lett.* **12**, 323–325 (2000)
31. Manolatou, C., Khan, M. J., et al.: Coupling of modes analysis of resonant channel add drop filters. *IEEE J. Quantum Electron.* **35**, 1322–1331 (1999)
32. Prkna, L., Čtyroký, J., et al.: Ring microresonator as a photonic structure with complex eigenfrequency. *Opt. Quantum Electron.* **36**, 259–269 (2004)
33. Taflov, A., Hagness, S. C.: *Computational Electrodynamics: The Finite Difference Time Domain Method*, 2nd ed. Artech House, Norwood, MA, USA (2000)
34. Hagness, S. C., Rafizadeh, D., et al.: FDTD microcavity simulations: Design and experimental realization of waveguide coupled single mode ring and whispering gallery mode disk resonator. *IEEE J. Lightw. Technol.* **15**, 2154–2165 (1997)
35. Koos, C., Fujii, M., et al.: FDTD-modelling of dispersive nonlinear ring resonators: Accuracy studies and experiments. *IEEE J. Quantum Electron.* **42**, 1215–1223 (2006)

36. Sacks, Z. S., Lee, J.-F.: A finite-element time-domain method using prism elements for microwave cavities. *IEEE Trans. Electromagn. Compat.* **37**, 519–527 (1995)
37. Carpes Jr., W. P., Pichon, L., et al.: Efficient analysis of resonant cavities by finite element method in the time domain. *IEE Proc. Microw. Antennas Propag.* **147**, 53–57 (2000)
38. Ji, X., Lu, T., et al.: Discontinuous galerkin time domain (DGTD) methods for the study of 2-D waveguide-coupled microring resonators. *IEEE J. Lightw. Technol.* **23**, 3864 – 3874 (2005)
39. Boriskina, S. V., Benson, T. M., et al.: Effect of a layered environment on the complex natural frequencies of two-dimensional WGM dielectric-ring resonators. *IEEE J. Lightw. Technol.* **20**, 1563–1572 (2002)
40. Boriskina, S. V., Benson, T. M., et al.: Highly efficient design of spectrally engineered whispering-gallery-mode microlaser resonators. *Opt. Quantum Electron.* **35**, 545–559 (2003)
41. Boriskina, S. V., Nosich, A. I.: Radiation and absorption losses of the whispering-gallery-mode dielectric resonators excited by a dielectric waveguide. *IEEE Trans. Microw. Theory Tech.* **47**, 224–231 (1999)
42. Jackson, J. D.: *Classical electrodynamics*. John Wiley and Sons, Inc., 3rd edition (1998)
43. Lewin, L., Chang, D. C., et al.: *Electromagnetic Waves and Curved Structures*. Peter Peregrinus Ltd. (On behalf of IEE), Stevenage, England (1977)
44. Pennings, E. C. M.: *Bends in Optical Ridge Waveguides, Modelling and Experiment*. Ph.D. thesis, Delft University, The Netherlands (1990)
45. Abramowitz, M., Stegun, I. A.: *Handbook of Mathematical Functions (Applied Mathematics Series 55)*. National Bureau of Standards, Washington, D.C. (1964)
46. Press, W. H., Teukolsky, S. A., et al.: *Numerical Recipes in C, 2nd ed.* Cambridge University Press (1992)
47. Hiremath, K. R.: *Coupled mode theory based modeling and analysis of circular optical microresonators*. Ph.D. thesis, University of Twente, The Netherlands (2005)
48. Stoffer, R.: *Uni- and Omnidirectional Simulation Tools for Integrated Optics*. Ph.D. thesis, University of Twente, Enschede, The Netherlands (2001)
49. Sudbø, A. S.: Film mode matching: a versatile numerical method for vector mode fields calculations in dielectric waveguides. *Pure Appl. Opt.* **2**, 211–233 (1993)
50. Prkna, L., Hubálek, M., et al.: Vectorial eigenmode solver for bent waveguides based on mode matching. *IEEE Photonics Technol. Lett.* **16**, 2057–2059 (2004)
51. Hiremath, K. R., Hammer, M.: Modeling of tuning of microresonator filters by perturbational evaluation of cavity mode phase shifts. *IEEE J. Lightw. Technol.* **25**, 3760–3765 (2007)

Index

- Bent waveguides
 - Phase constant, 9
 - Propagation constant, 9
- Bent waveguides
 - 2D Analytical model, 9
 - 3D Film mode matching (FMM), 24
 - Attenuation constant, 9
 - Transverse electric (TE) mode, 9
 - Transverse magnetic (TM) mode, 9
- Coupled mode equations, 14
 - Variational formulation, 13
- Coupled mode theory, 2, 12
- Couplers
 - 2D Bent-straight waveguide, 12
 - 3D Bent-straight waveguide, 25
 - Scattering matrix, 4, 5, 14
 - Transfer matrix, 14
- Finite difference time domain (FDTD) method, 3
- Finite element method
 - Discontinuous Galerkin, 3
- Free spectral range (FSR), 8
- Full width at half maximum (FWHM), 8
- Integral equation methods, 3
- Projections, 15
- Quality factor, 8
- Reciprocity
 - of scattering matrix, 5
 - Identity, 14
- Resonance condition, 6, 7
- Spectrum evaluation
 - Constant scattering matrix method, 20
 - Direct method, 19
 - Reduced scattering matrices method, 20
- Standard resonator model, 3, 4
- Time domain cavity modes, 2
- Uniform asymptotic expansions, 9, 10
- Whispering gallery modes (WGM), 10